UNIVERSITY OF
BATH

Citation for published version:
Casanova, S, Liu, TY, Chew, J, Livingston, AG & Mattia, D 2020, 'High flux thin-film nanocomposites with embedded boron nitride nanotubes for nanofiltration', *Journal of Membrane Science*, vol. 597, 117749. https://doi.org/10.1016/j.memsci.2019.117749

DOI:
10.1016/j.memsci.2019.117749

Publication date:
2020

Document Version
Peer reviewed version

Link to publication

Publisher Rights
CC BY-NC-ND

University of Bath

Alternative formats
If you require this document in an alternative format, please contact:
openaccess@bath.ac.uk

1 # High Flux Thin-Film Nanocomposites with Embedded Boron Nitride

2 # Nanotubes for Nanofiltration

3 *Serena Casanova,†‡ Tian-Yin Liu, § Yong-Min J. Chew,†‡ Andrew Livingston,§** Davide Mattia†‡**

4 †Department of Chemical Engineering, University of Bath, BA2 7AY, UK

5 ‡Centre for Advanced Separations Engineering, University of Bath, BA2 7AY, UK

6 §Department of Chemical Engineering, Imperial College London, South Kensington Campus, SW7 2AZ, UK

7 **Department of Engineering and Material Sciences, Queen Mary University of London, London E1 4NS, UK

8

9 * Address correspondence to d.mattia@bath.ac.uk

10 ## Abstract

11 A novel thin film nanocomposite (TFN) membrane was obtained by incorporating boron nitride

12 nanotubes (BNNTs) into a polyamide (PA) thin selective layer prepared via interfacial

13 polymerisation. The addition of just 0.02 wt% of BNNTs led to a 4-fold increase in pure water

14 permeance with no loss in rejection for divalent salts, methylene blue or humic acid compared

15 to the pure PA membrane. Loadings higher than 0.02 wt% of BNNTs led to agglomeration

16 with overall loss of performance. For the membranes containing 0.02 wt% BNNTs, the pure

17 water permeance was 4.5 LMH@bar, with > 90% rejection of $MgSO_4$ and > 80% rejection of

18 $CaCl_2$. Fouling tests with humic acid showed a flux recovery ratio of > 95% with ~50% lower

19 flux loss during the fouling cycle compared to the polyamide only membrane. These values

20 represent a significant improvement over both commercial polyamide membranes and TFN

21 membranes incorporating carbon nanotubes. We assert that the very small quantity of BNNTs

22 needed to produce the enhanced performance opens the way to their use in water treatment

23 applications where nanofiltration membranes are subject to severe organic fouling.

24

25

26 **Keywords:** Boron nitride nanotubes; Chemical vapour deposition; Interfacial Polymerisation; Nanofiltration

27

1. Introduction

Polymeric nanofiltration (NF) membranes have become a mainstay of water treatment processes, with high recovery rates [1], facile modular scale up [2] and economic viability across a broad range of feed [3]. NF membranes are particularly effective for the combinatorial rejection of salts, organic compounds, natural organic matter (NOM), and dyes. [4]. Industry, however, still faces challenges including high energy costs per unit volume of water purified [5], handling of retentate waste [6], membrane fouling, and a fundamental understanding of the mechanisms underlying the purification of complex feeds [7].

Thin-film composite (TFC) membranes composed of a very thin, dense selective layer supported by a porous support combine high flux and rejection with mechanical stability. Although TFC membranes are successfully used commercially [8], there is still need to increase efficiency, reduce energy consumption and extend chemical stability [9]. Many approaches have been explored to improve the performance of TFCs, including diverse fabrication methods, and the tuning of precursors used to fabricate the membranes [10]. Another promising strategy is the incorporation of inorganic nanomaterials in the thin selective layer to form so-called thin-film nanocomposite (TFN) membranes [7]. Nanomaterial additions alter the structure of the selective layer by finely tuning properties such as hydrophilicity [11], porosity [12], surface zeta potential [13] and stability [14, 15]. Additionally, the nanomaterials can introduce desired features such as fouling resistance [16], adsorption [17] and photocatalytic characteristics [18] into the membranes.

Amongst the wide range of nanomaterials tested to date [2], carbon nanotubes (CNTs) have been considered for application in membrane technology due to their fast water transport and low tortuosity [19]. The reduced friction of water on the defect-free carbon surface in these nanotubes results in very high water permeances through the tubes [20], translating into higher efficiency (i.e. higher flux) per applied pressure [21]. However, efforts to create membranes with the CNTs aligned perpendicularly to the membrane's surface in a commercially scalable fashion have been have been, so far, unsuccessful [22-24]. On the other hand, the incorporation of randomly aligned CNTs in polymer matrices has led to the successful formation of selective membranes [25], but with only modest increases in water permeance and a decrease in selectivity [26, 27]. While the former can be attributed to the small fraction of tubes directly connecting feed and permeate, the latter is attributed to the formation of uncontrolled permeation pathways at the interface between the CNTs and the polymer, due to poor chemical

60 compatibility [28]. This aspect has been addressed by introducing an additional

61 functionalisation step with acid groups, to form hydroxyl and carboxyl groups on the tube

62 surface [29]. The functionalised CNTs have been added in relatively large amounts (1 wt% -

63 10 wt%), with a corresponding increase in rejection of up to 5% and providing permeances up

64 to 50% higher than those of the starting polyamide membrane [30, 31]. CNTs have also been

65 functionalised with more complex zwitterion groups. However, these have penalised the water

66 permeance when compared to pristine CNTs, though improving the rejection of NaCl from

67 97.6% to 98.5% thanks to the steric hindrance of the zwitterion functional groups [32]. Despite

68 these promising results, the potential for permeance increase is limited by the low loadings of

69 hydrophobic nanomaterials that can be incorporated into the membrane matrix before the onset

70 of agglomeration, which leads to the formation of pinholes, with a subsequent loss of

71 performance [33].

72 Herein, boron nitride nanotubes (BNNTs) are investigated as nanomaterials for TFN

73 fabrication. We speculate that their physico-chemical characteristics will overcome some of

74 the limitations of CNT-based TFNs highlighted above. Hexagonal BNNTs (*h*BN) are

75 isostructural to graphitic CNTs, but behaving as electrical insulators and showing higher

76 resistance to oxidation [34]. Molecular dynamics simulations on BNNTs in the subcontinuum

77 range, with diameters 0.8 nm, have shown faster pure water flux than in CNTs [35]. For such

78 small diameters it was shown that increased van der Waals and electrostatic interactions

79 between the nanotube walls and the water molecules contribute to an easier filling of the bore

80 of BNNTs than for CNTs [36]. However, when the diameters of the tubes studied were larger,

81 CNTs outperformed BNNTs in terms of improved water fluxes [37]. This was ascribed to

82 differences in the electronic landscape in the two nanotube walls [38]. Simulations also showed

83 that BNNTs have tunable cation and anion selective properties due to the partial charge on the

84 boron and nitrogen atoms of the nanotube [39] and osmotic energy storage capabilities [40].

85 Additionally, when boron nitride nanosheets were recently embedded in mixed matrix

86 membranes, they showed improved fouling resistance [26]. Boron nitride nanotubes have

87 recently been used to fabricate ultrafiltration membranes with improved thermal resistance and

88 mechanical stability [41]. Moreover, CNTs have been shown to have antioxidant capabilities

89 that slow down chlorine attack on polymeric membranes [28], however this effect is as yet

90 unreported for BNNTs. Using BNNTs as membrane nanofillers is motivated, together with its

91 novelty, by the fact that materials with high negative zeta potentials allow for rejection of

92 pollutants not only by size but also by charge [42].

3

93 Despite the many potential advantages of BNNTs over CNTs, there has been notably less
94 published research on BNNTs than on their carbon counterparts, attributed mainly to the lack
95 of methods for the production of BNNTs at scale [34]. This obstacle has been overcome in this
96 work, optimising a known technique [43] for the production of BNNTs by chemical vapour
97 deposition (CVD). The nanomaterial was then embedded in the selective phase of an
98 interfacially polymerised polyamide (PA-BNNT) membrane. BN is negatively charged in
99 water over a broad pH range [44] and can adsorb OH^- on its surface further increasing its
100 negative charge [40].

2. Materials and Methods

2.1 Materials

103 Boron (B, $\geq$ 95%), magnesium oxide (MgO, $\geq$ 99.99%), iron oxide (Fe_2O_3, $\geq$ 99.9%) and MgO
104 nanopowder (average particle size $\leq$ 50 nm, measured by BET [45]) were purchased from
105 Sigma Aldrich. Ethanol ($\geq$ 99%) was purchased from Fisher Scientific. P-type silicon wafers
106 polished on one side were purchased by Agar Scientific. Hydrochloric acid (38%) was
107 purchased from Sigma Aldrich. Commercial polyether sulfone (PES) membrane Microdyn
108 Nadir PMUP010 with 10 kDa nominal molecular weight cut-off was purchased from Steriltech.
109 Deionised (DI) water was used unless specified otherwise. Methanol (MeOH, anhydrous,
110 99.8%), Piperazine (PIP, 99%) ReagentPlus®, with MW86, n-hexane (anhydrous, 95%) and
111 trimesoyl chloride (TMC, 99%) were purchased from Sigma Aldrich. Diiodomethane (DIM,
112 99%) was purchased from Sigma Aldrich. Salts (*e.g.*, NaCl, $CaCl_2$ and $MgSO_4$) were purchased
113 from Sigma Aldrich. Sodium hypochlorite technical solution was purchased from Fischer
114 Scientific.

2.2 BNNTs synthesis

116 BNNTs synthesis (Fig. 1) with ammonia gas and boron powder precursors was catalysed by
117 Fe_2O_3 and MgO catalysts with a molar ratio of B:MgO:Fe_2O_3 = 2:1:1. B, MgO and Fe_2O_3 were
118 pre-mixed at 250 r.p.m. for 12 h in a Fritsch Pulverisette P6 planetary ball mill, half filling a
119 45 ml stainless steel grinding bowl with 2.2 g of B, MgO and Fe_2O_3 in an ethanol suspension
120 and 18 grinding balls with 5 mm diameter. After ball milling, 5 ml of precursor was poured in
121 a Coors™ alumina combustion boat, which was then capped with a silicon wafer previously
122 seeded with MgO nanopowder. The closed boat was then placed in a 15 cm long quartz test

tube (ID 18 mm, OD 19 mm) facing the gas inlet in the centre of a quartz tube reactor (H-Baumbach, ID 20 mm, OD 22 mm) in a three sections horizontal TZF 12/38/850 type CARBOLITE tubular furnace. Temperatures inside the furnace were monitored by external thermocouples. Gas flows were controlled with Omega FMA 5400A/5500A series mass flow controllers (MFCs) regulated by a LabVIEW program. The tube reactor was abundantly flushed with Ar and then let ramp up at 10 °C/min up to 1100 °C under a 200 sccm Ar flow. Then, the gas flow was switched to 145 sccm NH_3 and the temperature increased to 1200 °C at the same heating rate. This maximum temperature was kept for 1 hour before letting the system cool down to room temperature under a 200 sccm Ar stream. The exhaust NH_3 gas was neutralized with a sulphuric acid scrubber, generating ammonium sulphate salts. The BN nanotubes white powder was gently removed with a stainless steel spatula by scratching it from the silicon substrate and boat top and sides. The unreacted boron in the collected white powder was removed in air at 700 °C for 2 hours, where it reacted to form boric anhydrite vapour. BNNTs have high thermal stability and are resistant to oxidation up to 950 °C [45]. Catalysts were removed with a 3 hours 10% HCl (purity 36.5-38.0%, purchased from Sigma Aldrich) water cleaning at 40 °C, followed by washing of the products in DI water by vacuum filtration using a 0.45 µm pore size nylon membrane (Pall Corporation).
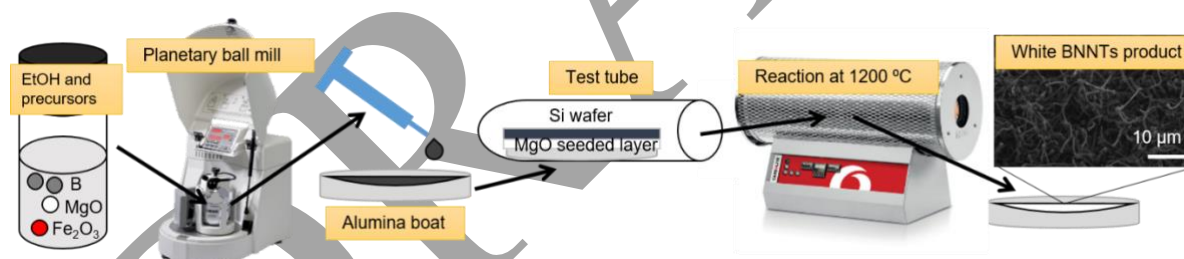
Fig. 1 Schematic of the CVD of boron nitride nanotubes production.

2.3 Polyamide membrane fabrication

The PA-BNNTs membranes were synthesized by interfacial polymerisation following an established vacuum filtration technique [46], which has been recently used for the fabrication of nanocomposite membranes [47]. The PES support membrane (Microdyn Nadir PMUP010) was cut in discs with 5.5 cm in diameter, and then flushed with 20 ml of water in a filtration setup prior to synthesis. Then, 1 wt% PIP aqueous solution (MeOH:H_2O 50:50 v/v%) solution was prepared by rapidly dissolving the PIP flakes. For the PA-BNNT membranes, 0.01, 0.02 or 0.03 wt% BNNTs were dispersed in the amine solution by ultrasonication for 1 h (Table 1). Then, 25 ml amine solution or amine solution with dispersed BNNT was pumped through the

support membrane until the entire amount of solution was filtered, while ensuring the membrane remained wet. Subsequently, any residual drops on the side of the wetted membrane were removed by using an air gun to avoid the formation of defects in the resulted amine-rich film. In the interfacial polymerisation, a 0.8 wt% TMC n-hexane solution statically contacted the amine-saturated support in the filtration setup. The reaction time was 3 min. The residual organic solution was discarded, and the membrane was quenched with n-hexane for 1 min. After reaction, the membrane was left to dry at room temperature for 24 h. Similarly, a thin film was formed by contacting 1 ml of PIP solution with 1ml of TMC solution, specifically for the analysis of a free standing film at the interface.

Membranes with different concentration of BNNTs in the starting solution were prepared; their nomenclature, PIP solution composition, and the estimated weight of nanofiller deposited per unit area by filtering 25 ml of amine solution are reported in Table 1. The concentrations to be investigated were chosen in a range where no obvious large agglomeration could be observed on the membrane top surface with the naked eye. It should be noted that there is an uncertainty in the estimation of the amount of BNNTs per unit area, due to the possibility that some minor fraction of nanomaterial filtered through the PES support.

Table 1 Composition of the PIP solutions in MeOH:H_2O 50:50 v/v% for the PA-BNNTs membranes.

Membrane	PIP (wt%)	MeOH/H_2O (wt%)	BNNTs (wt%)	c_S (mg/cm2)
PA-BARE	1.00	99.00	0.00	0.000
PA-BNNTs0.01	1.00	98.99	0.01	0.096
PA-BNNTs0.02	1.00	98.98	0.02	0.193
PA-BNNTs0.03	1.00	98.97	0.03	0.283

2.4 Characterisation of BNNTs powders

The produced nanotubes were coated with 5 nm of chromium and positioned on carbon tape for analysis with a JEOL JSM-6301F FESEM at 5kV. JEOL JSM-2100Plus TEM samples were prepared by dispersing the nanotubes in ethanol. Two to five drops of the sample were then placed on a TEM window (Lacey carbon purchased from EM Resolutions) until a desirable concentration was reached. Analysis of structural features with ImageJ was done on a minimum of 10 measurements. Optical Images of the substrates with BNNTs grown on them were taken with a Digital Microscope VHX-6000 series. Raman spectroscopy was carried out on the as-synthesized samples on a glass slide in a Renishaw Raman Microscope series 1000 using a frequency-doubled argon ion laser (wavelength 244 cm-1, 5.08 eV) with spectral resolution of

179 5 - 10 cm-1 and a $40 \times$ UV objective lens. XRD tests of products of the synthesis were reduced

180 into fine powders dispersed on a silicon wafer were carried on 1 mg of product with a Bruker

181 D8 Advance for $10 < 2\theta < 70$ with a Vantec detector with Cu K-alpha radiation.

182 XPS was performed on powdered BNNTs samples using a Thermo Fisher Scientific K-alpha+

183 spectrometer. Samples were analysed using a micro-focused monochromatic Al x-ray source

184 (72 W) over an area of approximately 400 microns. Data was recorded at pass energies of 150

185 eV for survey scans and 40 eV for high resolution scan with 1 eV and 0.1 eV step sizes

186 respectively. Charge neutralisation of the sample was achieved using a combination of both

187 low energy electrons and argon ions. Data analysis was performed in CasaXPS using a Shirley

188 type background and Scofield cross sections, with an energy dependence of -0.6.

189 *2.5 Polyamide membrane characterisation*

190 Membranes were coated with 10 nm of Cr before imaging in a JEOL JSM-6301F FESEM.

191 Micrographs were taken at 5kV. Atomic Force Microscopy (AFM) Nanosurf EasyScan 2 Flex

192 scans were taken by using the Dynamic Force Mode with a 190Al-G tip on areas 5 µm $\times$ 5 µm

193 with 256 points/line. The data was analysed with Gwyddyion and the software's internal

194 functions were used to assess the membrane's average roughness (R_a). Dataphysics Optical

195 Contact Angle (OCA) Measuring Device with 0.5 µl wetting liquid drops was also used to

196 characterise the membranes. The Young's contact angle (θ_Y) on a flat smooth surface is related

197 to the measured contact angle (θ_W) via the Wenzel equation [48]:

$$cos\theta_W = r \, cos\theta_Y, \tag{1}$$

198 where r is the ratio between the membrane surface area and the projected area, obtained by

199 AFM.

200 The surface zeta potential of samples with dimensions 2×1 cm or 1×1 cm was measured in

201 a SurPASS electrokinetic analyser with adjustable gap cell in a pH range between 3 and 10.

202 For each pH value, the measurement was repeated four times. A Perkin Elmer Spectrum FTIR-

203 ATR Spectrometer was used to characterise the membranes' selective layer surface, with 16

204 scans per run between 600 and 4000 cm-1 and a spatial resolution of 2 cm-1.

205 Sections of the polyamide membranes top surface measuring 1 cm $\times$ 1 cm were also analysed

206 by XPS. The ratio O/N from the XPS analysis was measured to assess the degree of

207 crosslinking in relation to loading percentage. This was calculated from

$$crosslinking~(\%) = \left(\frac{(O/N)_{XPS} - (O/N)_{fully~cross-linked}}{(O/N)_{fully~linear} - (O/N)_{fully~cross-linked}} \right), \tag{2}$$

208 where $(O/N)_{XPS}$ is the oxygen to nitrogen ratio obtained experimentally, neglecting the 398

209 eV contribution of the hBN nitrogen [49]. $(O/N)_{fully~linear}$ and $(O/N)_{fully~crosslinked}$ are the

210 ratios for a fully linear and fully crosslinked polyamide, respectively [50].

211 Phillips CM200 TWIN TEM samples were prepared by gently depositing a thin film on a TEM

212 window and imaging it at 250 and 25k magnification.

2.6 Membrane filtration performance

214 Pure water flow was tested in cross flow mode (schematics in [26]) on a minimum of three

215 membranes per composition, with 24 h of compaction at 7 bar and three days of testing at 3

216 bar.

217 Dye and salts rejection was tested for 7 h with a 45 L h-1 pump flow rate. Rejection of methylene

218 blue was assessed using a UV spectrophotometer (UV Cary 100, Agilent, U.K.), while rejection

219 of the salts was measured using an Orion Versastar ThermoScientific conductivity meter. The

220 feed concentration for the dye tests was 0.01 g L-1, whilst for salts rejection it ranged from 500

221 to 2000 ppm.

222 Humic acid fouling tests were performed on pre-compacted membranes in cross flow mode.

223 The 2.5 L feed of 1 g L-1 humic acid in water was prepared beforehand and mixed with a

224 magnetic stirrer for 24 hours before the test. The fouling test consisted of two fouling cycles of

225 15 hours and two cleaning cycles of one hour each. The flow rate was set as 175 ml min-1

226 (Reynolds number, $Re = 130$) and 750 ml/min ($Re = 550$) for fouling and cleaning respectively.

227 Flux recovery ratio (FRR) was measured before each cycle as follows:

$$FRR~(\%) = \left(\frac{J_{AF}}{J_{BF}} \right) \times 100 , \tag{3}$$

228 where J_{BF} and J_{AF} are the two fluxes before fouling and after cleaning, calculated for each

229 cycle.

230 The membrane total resistance (R_t) after 15 hours of fouling test was also calculated:

$$R_t = R_m + R_r + R_{ir}, \tag{4}$$

8

with R_m, R_r and R_{ir} being the intrinsic membrane resistance and the reversible and irreversible fouling resistance, respectively. These are calculated by using:

$$R_m = \frac{\Delta P}{\mu \times J_{BF}};$$
(5)

$$R_{ir} = \frac{\Delta P}{\mu \times J_{AF}} - R_m;$$
(6)

$$R_r = \frac{\Delta P}{\mu \times J_F} - R_m - R_{ir}.$$
(7)

The transmembrane pressure is indicated with ΔP and the viscosity with μ, while J_F is the flux in m3 s-1 of humic acid after 15 hours of fouling. The term $R_{\%}$ was used to assess the extent of reversible fouling in each membrane during fouling tests:

$$R_{\%} = \frac{R_r}{R_t} \times 100.$$
(8)

The first 10 ml of permeate were discarded in every test, to account for dead volume and permeate tubing. The mass balance for the rejection of component i is so calculated:

$$mass\ balance\ (\%) = \frac{V_{P,i} c_{P,i} + V_{R,i} c_{R,i}}{V_{F,i} c_{F,i}} \times 100,$$
(9)

where the subscripts P, R and F stand for permeate, feed and retentate respectively; V is the volume and c the concentration.

Chlorine resistance tests were performed with 4 L feed water containing 2000 ppm NaOCl and 2000 ppm CaCl2. Rejection and permeance were monitored over a period of 5 hours and 30 minutes, while the membranes were tested in cross flow mode with a pump velocity of 45 L h-1 at 3 bar. Membranes were pre-compacted before rejection tests.

3. Results and Discussion

3.1 BNNTs synthesis

BNNTs were synthesized via chemical vapour deposition, resulting in a dense product (Fig. 2a), with the BNNTs having open ends (Fig. 2b) and homogenously grown over the entire substrate area (Fig. 2c) with a vertical orientation (inset cross-sectional HRTEM). The BNNTs powder was collected with a yield of ~10 mg per run by simple scratching of the silicon wafer (W x L 14 x 70 mm) substrate. The diffraction pattern generated by a single tube (Fig. 2d) confirmed the *h*BN (002) crystal structure of boron nitride multiwalled (wall thickness ~4.5 nm) nanotubes [51], with a straight inner channel of *c.a.* 8 nm in diameter and an outer diameter of *c.a.* 17 nm (Fig. 2e) where the interspace layer distance of *h*BN is 0.328 nm as expected from literature [34]. Combining the open ends and penetrating inner voids, the as-synthesized BNNTs are ideal candidates for creating nanoscale channels in TFN membranes [52]. The morphology of the BNNTs showed a relatively wide size distribution with outer diameters in the range of 5 to 105 nm and tube lengths in the range of 1 to 5 μm, as statistically counted by 200 tubes in TEM micrographs (Fig. 2f).
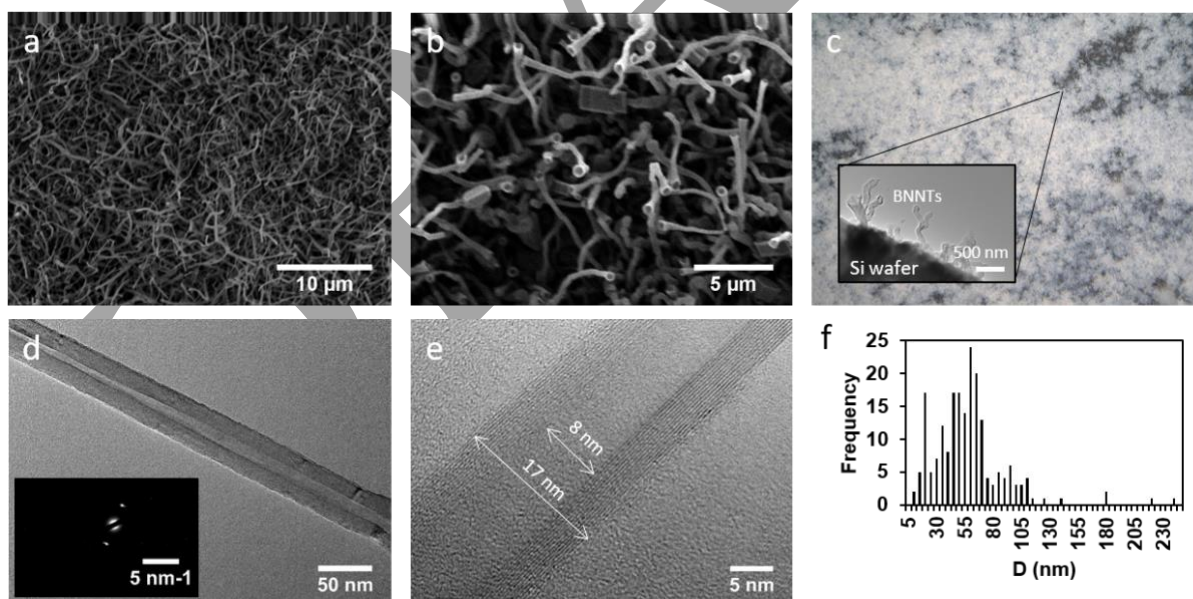
Fig. 2 (a) FESEM micrograph of BNNTs on the Si wafer taken at 3000 x magnification and **(b)** collected from the alumina boat taken at 5000 x magnification with 8 mm working distance. **(c)** Optical microscope image (500 x) with a TEM micrograph inset showing BNNTs grown on a piece of silicon wafer; TEM micrographs and **(d)** corresponding diffraction pattern and **(e)** measures for inner and outer tube diameter of a selected BNNT tube where the *h*BN interlayer spacing can be observed. **(f)** Counts of outer diameter intervals for 200 tubes randomly imaged with TEM.

269   The BNNTs powder samples present the typical Raman hBN peak at 1369 cm-1 (Fig. 3a). The

270   XRD spectra in Fig. 3b shows four main BN peaks at 2θ = 10.5o (hBN 001), 29o (hBN 002),

271   40o (hBN 100) and 53o (hBN 004) [53], alongside some iron and MgO peaks in the region 20o

272   < 2θ < 40o, identified as catalyst impurities. Boron nitride FTIR peaks are identified in Fig. 3c

273   for the vibration mode along the tubes' longitudinal axis at 1367 cm-1, in the tangential

274   direction at 1537 cm-1 and the out of plane buckling mode at 795 cm-1 [43]. The spectra also

275   presents peaks attributed to Si-O in the 1130-1000 cm-1 region and Si-H in the 850-900 cm-1

276   region, as the spectra was taken before the BNNTs material was scraped from the Si substrate.

277   XPS results (Fig. 3d) identify a B/N atomic ratio of 1.18 in the powder BNNT sample, very

278   close to the theoretical value of 1. Peaks for hBN are identified at 190.41 eV and 398.00 eV

279   for B and N respectively, and a 3.75 at.% of N-B-O bonds can be observed in the B high

280   resolution spectra [49].

281
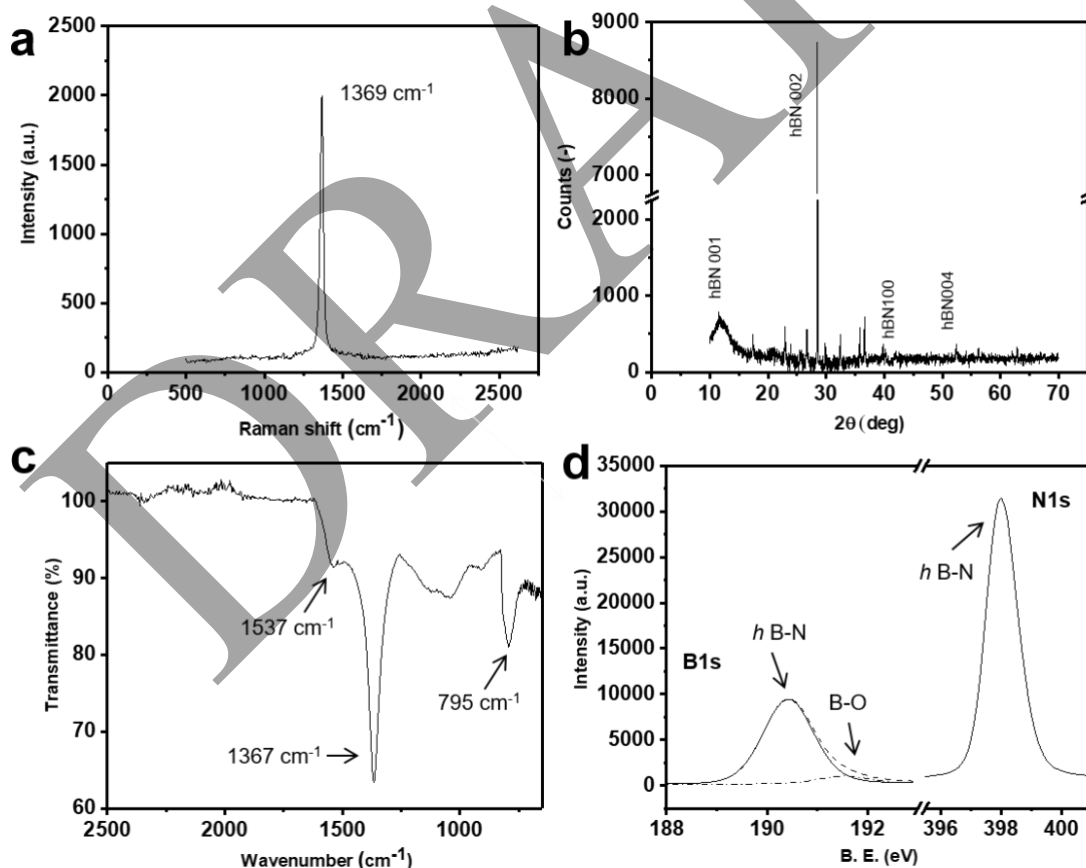
282

283   **Fig. 3 (a)** Raman analysis of BNNTs with the characteristic hBN peak at 1369 cm-1 and **(b)** XRD pattern of the

284   as produced BNNTs powder, showing four characteristic hBN peaks; **(c)** FTIR of BNNTs on silicon wafer; and

285   **(d)** B1s and N1s high resolution XPS spectra of the BNNTs.

11

3.2 Characterisation of PA-BNNTs membranes

287 The surface and cross-sectional morphologies of the produced polyamide membranes are

288 shown in Fig. 4. The irregular morphology increased with BNNTs loading, which is consistent

289 with an increase in the average surface roughness (R_a, nm) in Table 2, and therefore the ratio

290 between the membrane surface area and the projected area, r, and morphological changes

291 measured by AFM (Fig. 5). The crumpled areas observed in the PA-BNNTs membranes

292 showed similar material stiffness as the rest of the membrane (see phase plot analysis in **Error!**

293 **Reference source not found.**), indicating that no BNNTs protrude out of the membrane from

294 the top surface.
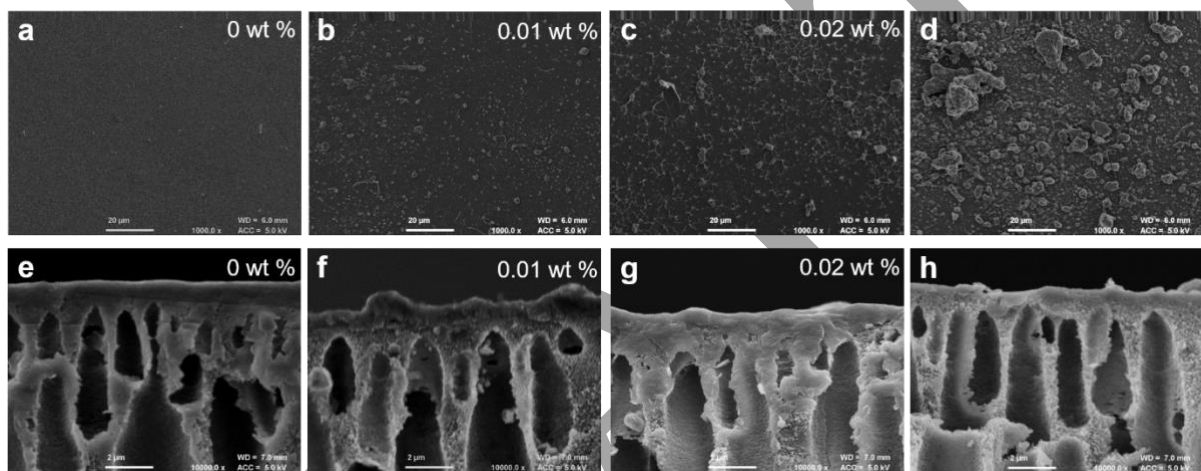
296 **Fig. 4** FESEM top and cross section of membranes prepared from solutions containing different percentages of
297 nanofiller: **(a,e)** bare, **(b,f)** 0.01 wt%, **(c,g)** 0.02 wt% and **(d,h)** 0.03 wt% PA-BNNTs membranes.
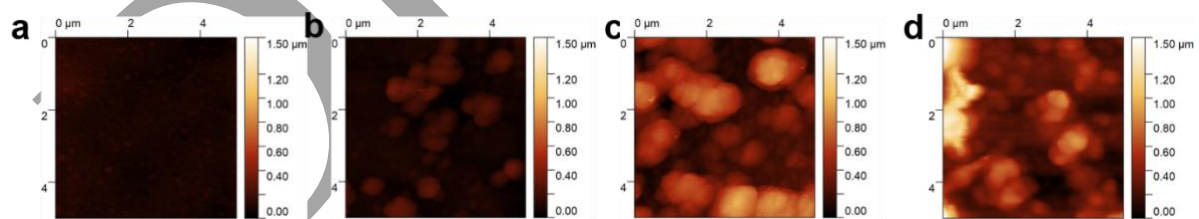
299 **Fig. 5** AFM maps of membranes **(a)** bare, **(b)** 0.01 wt%, **(c)** 0.02 wt% and **(d)** 0.03 wt% PA-BNNTs membranes.

300 Measured contact angle varies as a function of BNNTs concentration (Table 2). Water contact

301 angle increases by approximately 20o from PA-BARE to PA-BNNTs0.03, in agreement with

302 both the increase in roughness R_a already observed in Fig. 5 and an observed reduced material

303 hydrophilicity. When the measured contact angle and roughness are used to calculate values

304 for the Young's contact angles *via* the Wenzel equation [48], an observable although not drastic

305 increase in material hydrophilicity is observed, with Young's water contact angles increasing

by 15-20% for each 0.01 wt% of BNNT added. In contrast, the non-polar diiodomethane contact angle (θ_{Y_DIM}) decreased over the four membranes tested, in line with the loss of hydrophilicity of the membrane.

Table 2 Measured water (θ_{WATER}) and diiodomehtane (θ_{DIM}) contact angles, Young water (θ_{Y_WATER}) and diiodomehtane (θ_{Y_DIM}) contact angles obtained applying the Wenzel equation, average surface roughness R_a results on PA-BARE and PA-BNNTs membranes and ratio r between the membrane surface area and the projected area, obtained by AFM.

| Membrane	θ_{WATER}	θ_{DIM}	θ_{Y_WATER}	θ_{Y_DIM}	R_a	r
	(deg, $\pm 2°$)				(nm)	(-)
PA-BARE	25	30	35	39	19	1.11
PA-BNNTs0.01	32	29	40	38	49	1.11
PA-BNNTs0.02	30	28	49	48	172	1.32
PA-BNNTs0.03	45	10	59	44	181	1.37

A free-standing film was placed in the TEM to observe the embedment of the BNNTs in the polyamide (Fig. 6a). Wrinkles in the thin layer are created when this is transferred to the TEM grid, but these formations can be clearly differentiated from the BNNTs as these show a hollow nature as previously shown in Fig. 2 d,e and in the inset of Fig. 6a. Fig. 6b shows a picture of the polyamide thin film formed at the interface between the PIP H_2O/MeOH solution and TMC in hexane solution.
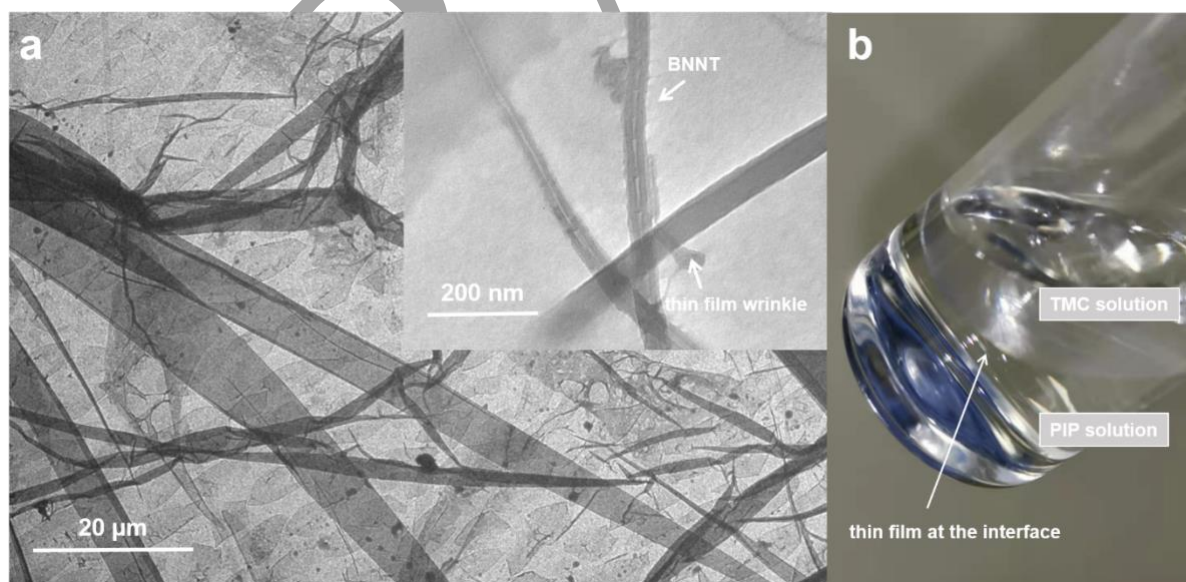
Fig. 6 (a) TEM micrograph of a free-standing film loaded with 0.01wt% BNNTs, observable in the magnified inset. Wrinkles generate in the film when it is transferred to the TEM grid. **(b)** Picture of a thin film produced at the interface between the TMC and PIP solutions.

As expected, the introduction of a negatively charged material in the texture of the IP membrane slightly decreased its surface zeta potential (Fig. 7). Although statistically significant (p-value=0.002), this change is not as dramatic as might be expected by the introduction of negatively charged nanomaterial, leading to the hypothesis that the vast majority of nanomaterial particles are surrounded by the selective polymer layer, and do not protrude from the top surface, consistent with the top layer stiffness results in **Error! Reference source not found.**.
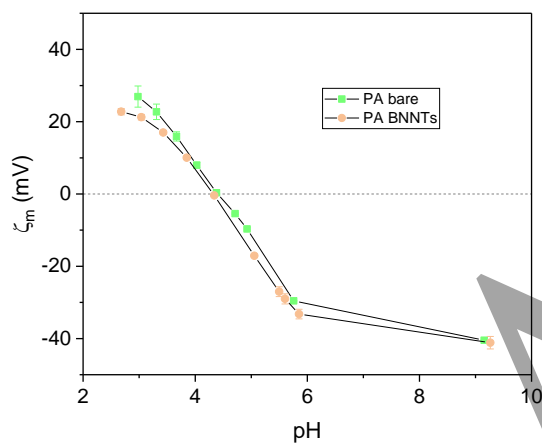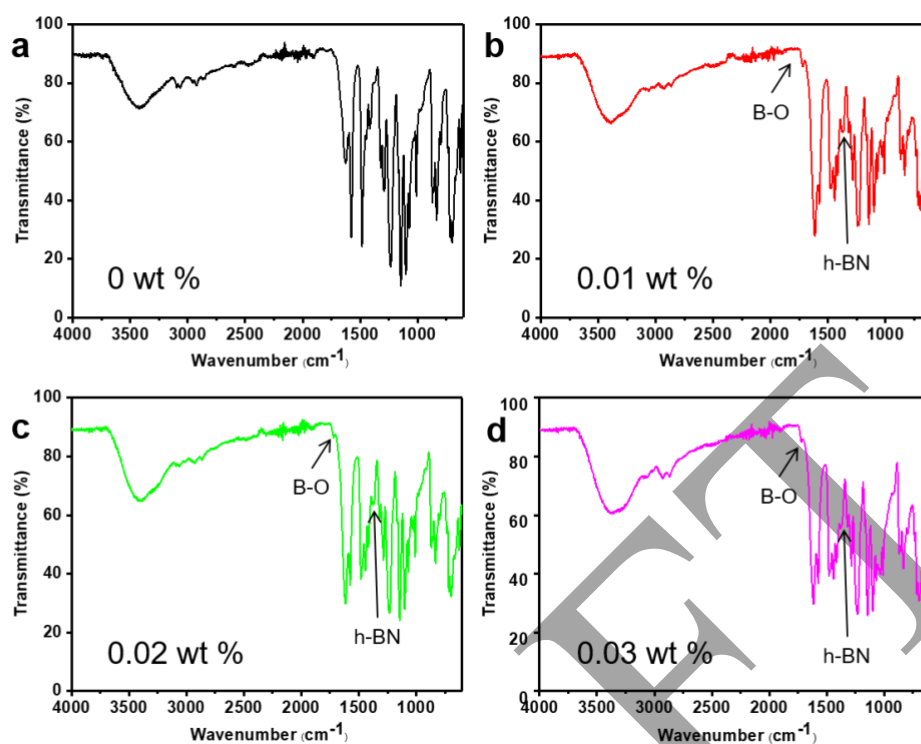

Fig. 7 Surface zeta potential (ζ_m) vs. pH of a PA-BARE (IEP=4.40) and PA-BNNTs0.01 (IEP=4.32).

Fig. 8 FTIR spectra for (a) bare, (b) 0.01 wt%, (c) 0.02 wt% and (d) 0.03 wt% PA-BNNTs membranes.

Fig. 8a reports the FTIR-ATR spectra for the IP BARE membrane [54], and Fig. 8b-c the scans for membranes with increasing BNNT loading. The beam penetrates the sample for 0.5 - 2 µm during testing [55], therefore representing the whole thickness of the membrane top layer and not just the very top surface. Thus, at the highest BNNTs concentration, the predominance of the 1375 cm$_{-1}$ BNNT' peak, corresponding to the longitudinal vibration mode of the tube, is observed [43, 56], together with a B-O functionalisation peak at 1721 cm$_{-1}$ [57], showing a new bond not observable in the FTIR for the BNNTs in powder form (Fig. 3c), and potentially indicating some interaction between the boron nitride and the polymeric matrix already visible for BNNTs concentrations of 0.01wt.%.

The O/N ratio for each membrane is reported in Table 3. A fully cross-linked polyamide, $(O/N)_{fully\ cross-linked}$, has a O/N ratio of 1 and a theoretically fully linear polyamide, $(O/N)_{fully\ linear}$, has a O/N ratio of 2 [50]. From these values, the degree of crosslinking was calculated from XPS results using Eq. (2). While the addition of 0.01wt% BNNTs increases the degree of crosslinking from 0.7 to 1.0, this declines moving to 0.02wt% and 0.03wt%, seemingly increasing the density of transport pathways available in selective layer [58].

15

Table 3 Experimental O/N from XPS and degree of crosslinking.

| Membrane	$(O/N)_{XPS}$	$crosslinking$ (%)
PA-BARE	1.3	0.7
PA-BNNTs0.01	1.0	1.0
PA-BNNTs0.02	1.6	0.4
PA-BNNTs0.03	1.7	0.3

3.3 Filtration performance of PA-BNNTs membranes: permeance, rejection and fouling

The permeance of the IP membranes evaluated increases with BNNT loading (Fig. 9a), from an average of 1.1 LMH/bar for the bare membrane to 2.7 LMH/bar for the PA-BNNTs0.01, 4.5 LMH/bar for the PA-BNNTs0.02 and 4.1 LMH/bar for PA-BNNTs0.03. The permeance values hints at a convex profile, often found in literature as a function of loading, as the initial addition of nanomaterial generates an initial increase in pore size, and then a decrease [29]. The former is ascribed to the higher free volume provided by the BNNTs [59], whereas the latter is due to increasing agglomeration [60]. The increase in water flow pathways however does not impact the membrane's rejection performance up to 0.02 wt% loading, most likely because the polyamide layer is still the main contribution to rejection up to that concentration value [59]. This suggests that the addition of the BNNT fillers might have created additional pathways for facile transport of water but not solutes [61, 62], and the slight increase in membrane surface charge might also have contributed to maintain a high rejection [2]. The slight decrease observed in the permeance value from PA-BNNTs0.02 to PA-BNNTs0.03 does not, however, show a statistically significant difference (Student's *t*-test, *p*-value > 0.05).

Two batches of PA-BNNTs membranes (empty and filled symbols in Fig. 9a) were tested for monovalent NaCl and divalent (CaCl2, MgSO4) salts rejection. Calibration curves for these measurements are reported in **Error! Reference source not found.**-4, and ionic concentrations in **Error! Reference source not found.**. The rejection for NaCl remains low (20 – 40 %) for the whole concertation range investigated with 0.03 wt% BNNTs being the worst performing case. However the membranes perform well for divalent salts rejection, with the rejection for MgSO4 is above 90 % for loading up to 0.02 wt% BNNTs, whilst it decreases to ~ 80 % for PA-BNNTs0.03. CaCl2 rejection raises from 75 – 80 % for the bare PA membrane to 97% for the PA-BNNTs0.01 and then decreases to around 40 % with further addition of nanofiller. The mass balance for the rejection of salts was ≥ 96% for CaCl2 and NaCl, and ≥ 90% for MgSO4. In all cases, the addition of 0.03 wt% of BNNTs notably penalises the membranes rejection,

whilst the membranes show highly desirable performances for loadings ≤ 0.02 wt%, with PA-BNNTs0.02, in particular, combining the highest permeance (4.5 LMH/bar) with the highest divalent salt rejection. This is conceivably due to the additional free volume and thus water pathways offered by the presence of the BNNTs in the matrix, while the polyamide enveloping the nanomaterial provides salt rejection.
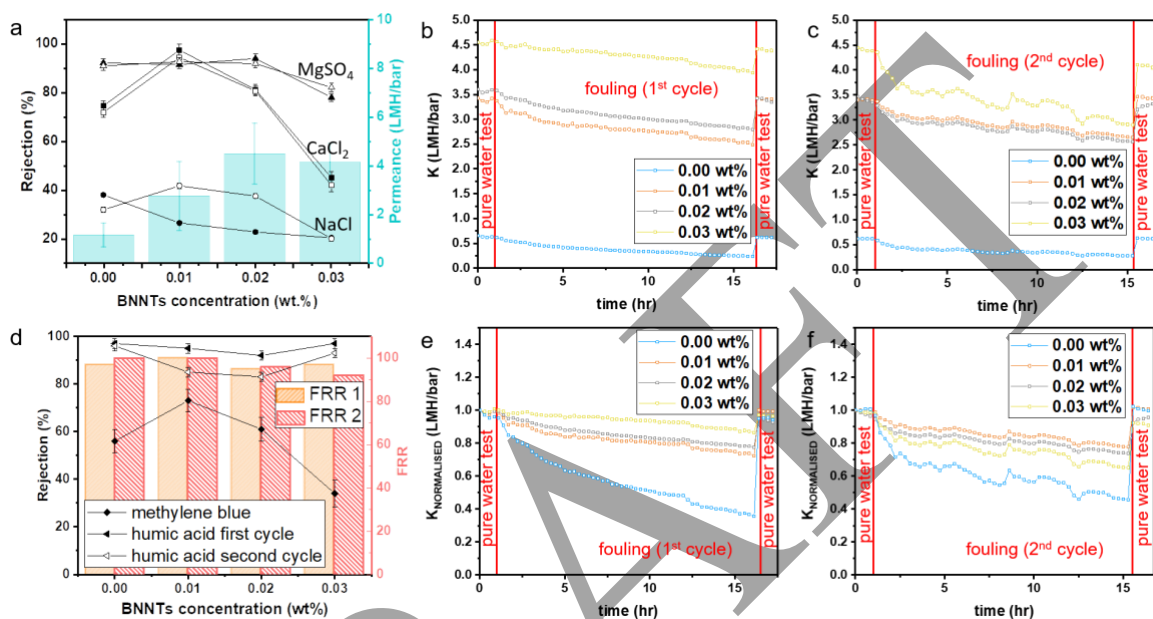
3.6

Fig. 9 (a) Salt rejection (left axis) and permeance (right axis) of the bare and TFN membranes containing BNNTs; rejection tests have been repeated on two batches of membranes indicated with full and empty dots for $MgSO_4$, $CaCl_2$ and NaCl: **(b)** First and **(c)** second fouling cycle; **(d)** Rejection of methylene blue (♦) and (◀,◁) humic acid together with flux recovery ratio (FRR) performances in the two fouling cycles in orange and red respectively; **(e)** first and **(f)** second fouling cycle, as displayed in the top panel, but normalised by initial pure water permeance for each membrane tested.

The observed behaviour showed little change in terms of recovering initial flux after two long fouling sequences in Fig. 9b and c, with high FRR: 97%, 100%, 95%, 97 % for the first cycle and 100%, 100%, 96, 92% in the second cycle for PA-BARE, PA-BNNTs0.01, PA-BNNTs0.02 and PA-BNNTs0.03, respectively. The membranes, possessing a white, opaque colour at the start, could be cleaned completely by vigorous water flushing and no irreversible contamination could be observed visually after the test or by the FRR results in the fouling cycles. The pump flow rate chosen in this study (175 ml min-1) is a common setting for membrane fouling tests [26]. However, this behaviour might change if the test was carried out at higher flows, where some irreversible fouling might be observed. However, Fig. 9e and f

17

explicitly show that PA-BARE reversibly fouls to a greater extent, decreasing to 40% of the initial flux, compared to 80-90% for the TFN membranes. This is possibly due to the absence of repulsion between the fouling material and nanofiller, which may lead to a higher percentage flux decline during tests, even though this is eventually recovered after cleaning. The contribution to total resistance during fouling can be observed in Fig.10.
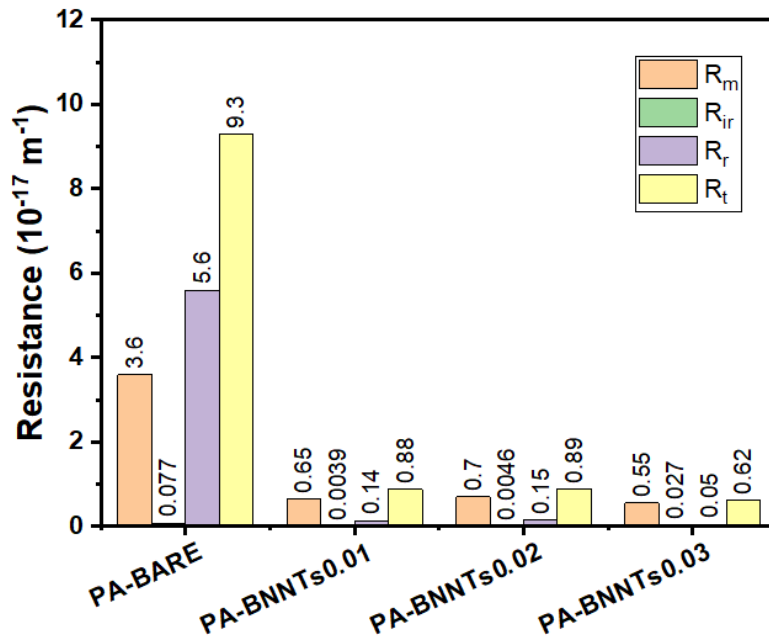
Fig. 10 Calculated membrane (R_m), irreversible (R_{ir}), reversible (R_r) and total (R_t) resistances for the membranes under analysis during the first fouling cycle.

The fouling layer resistance contribution to the total resistance decreased with increased BNNT loading, as indicated by the decrease in value of the parameter $R_{\%}$ for the first fouling cycle from 60.5% for PA-BARE to 8.0% for PA-BNNTs0.03 (**Error! Reference source not found.**). This can be observed in **Error! Reference source not found.** for the second fouling cycle as well, where, however, the benefit in terms of lower fouling layer resistance at high BNNTs loading is attenuated by a slightly lower FRR in PA-BNNTs0.02 and PA-BNNTs0.03.

Fig. 9d shows high rejection (80-90%) of humic acid in all the membranes tested (UV-vis calibration curve reported in **Error! Reference source not found.**). In addition to being able to effectively reject the foulant, all membranes could recover $\geq$ 95% of their initial flux, with PA-BNNTs0.03 recovering $\geq$ 90% of its flux after physical cleaning, indicating that the increased membrane roughness can make the removal of the formed fouling layer harder [4].

Fig.9d also reports data on the rejection of methylene blue dye, with the addition of 0.01 wt% BNNTs improving rejection by 17% compared to PA-BARE. Rejection then decreased with

422 increasing amounts of BNNTs added. As observed in the case of salts, the addition of 0.03 wt%

423 of BNNTs to the thin film worsens rejection performances. The mass balance for the rejection

424 of methylene blue was ≥ 96% for all samples.

425 The relation between rejection and $CaCl_2$ concentration in the operational range 500 - 2000

426 ppm was also studied (Fig. 11), with a stable selectivity between 500 and 1500 ppm. Above

427 this value, when Donnan type rejection becomes predominant [63] a decrease in rejection is

428 observed for the PA-BARE and PA-BNNTs0.03, but not for the PA-BNNTs0.01 and PA-

429 BNNTs0.02 for a concentration of $CaCl_2$ of 2000 ppm. When the PA layer is the major

430 contributor to rejection, however, a constant rejection over different concentrations is expected

431 [32]. We can therefore conclude that the PA layer is the major contributor to the rejection of

432 the membranes analysed, for all membranes but PA-BNNTs, where hypothesized defects due

433 to the high loading demonstrate a crucial concern particularly at high concentrations (2000

434 ppm).
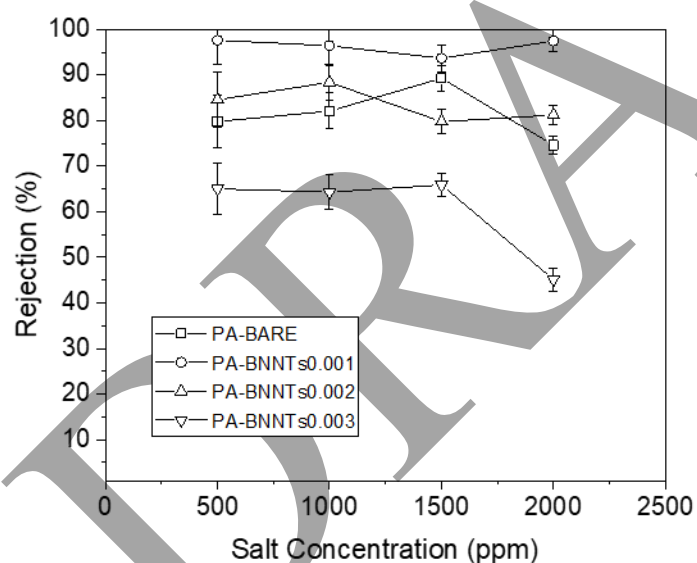
435

436 **Fig. 11** Dependence of $CaCl_2$ rejection on salt concentration for the membranes analysed in this work.

437 Membranes based on a polyamide linkage are prone to attack by chlorine in the feed, as free

438 chlorine radicals tend to be attracted by the N-H electron density [2]. Thus, NaOCl exposure is

439 studied here for the membranes under analysis. As observed in Fig. 12, the exposure to the

440 chlorinating agent is more adverse for all PA-BNNTs membranes compared to the PA-BARE,

441 indicating that the introduction of BNNTs in the polyamide structure exposes the amide bonds

442 prone to chlorine attacks. Previously it was found that increasing the density of amide bonds

443 in the PA membrane is a successful strategy for increasing chlorine resistance [64], and this is

consistent with the decrease in crosslinking in the PA-BNNTs membranes leading to premature failure in presence of NaOCl. In fact, at an exposure of 5000 ppm over 1 hr, while $CaCl_2$ rejection of PA-BARE decreased from 89% to 73%, PA-BNNT 0.01wt% plummeted from 97% to 32%. The permeance of PA-BNNTs 0.02wt% increased from 3.67 LMH/bar to 4.68 LMH/bar after 11000 ppm over 1 hr chlorine exposure. However, it remained fairly steady for the other membranes, indicating that the maximum exposure tested did not dissolve the PA layer, but was enough to perturb it and decrease notably its ion rejection.
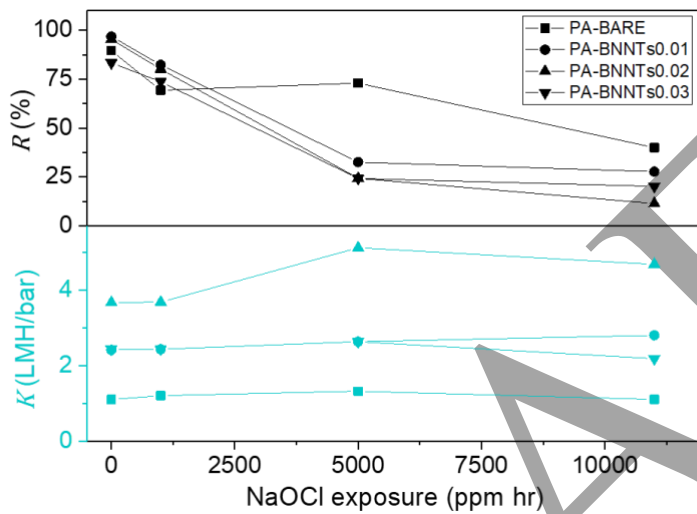
Fig. 12 Rejection (R) of $CaCl_2$ and permeance (K) of PA-BARE, PA-BNNTs0.01, PA-BNNTs0.02 and PA-BNNTs0.03 as a function of the exposure to sodium hypochlorite.

The best performing PA-BNNTs membrane in this work could provide 4 times higher permeance than PA-BARE membranes with only 0.193 mg cm-2 of nanofiller on the membrane area. For their part, hydroxyl functionalised CNT membranes were reported to show 2 times higher pure water permeance than thin film polyamide membranes, but required 13.3 mg cm-2 of filler [65]. An increase of permeance up to 2.7 times was reported in PA-CNTs, but this required the use of 0.458 mg/cm2 of modified MWCNTs. When compared with TFN membranes based on CNTs, the membranes in this work have therefore the capability to notably improve the permeance of pure polyamide using a limited amount of nanofiller (**Error! Reference source not found.**) and without requiring any additional functionalisation step.

Conclusions

In this work, a known synthesis route for the production of boron nitride nanotubes was optimised and deployed for the production of larger amounts of boron nitride nanotubes, which were then used as a nanofillers in nanofiltration thin film nanocomposite membranes prepared via interfacial polymerisation of PA. BNNTs homogeneously integrate in the polyamide layer, forming a B-O bond between the nanofiller and the polymer. Rejection of divalent and monovalent salts is not compromised for up to 0.02wt% BNNTs added to the aqueous phase in interfacial polymerisation, while the average permeance at this concentration goes up four times compared to the permeance of a membrane with no nanofiller. This is ascribed to an increase in water transport pathways given by the boron nitride nanochannels enveloped by the selective layer, with no appreciable loss of selectivity compared to the bare PA membrane. A permeance 4.5 times higher than in a bare PA membrane can be observed for low amounts of BNNTs, thus considerably limiting costs of adding nanofillers. Nonetheless, potential nanofiller leaching and recycling will have to be further investigated prior to large scale application, as BNNTs may be hazardous for the environment. In addition, the BNNTs membranes show a high resistance to irreversible fouling. This is a desirable condition for applications in, for example, the food industry, where standard operations take place in highly fouling environments.

Acknowledgments

References

[1] P. Xu, T.Y. Cath, A.P. Robertson, M. Reinhard, J.O. Leckie, J.E. Drewes, Critical review of desalination concentrate management, treatment and beneficial use, Environmental Engineering Science, 30 (2013) 502-514.

493 [2] J. Yin, B. Deng, Polymer-matrix nanocomposite membranes for water treatment, Journal
494 of membrane science, 479 (2015) 256-275.

495 [3] E. Jones, M. Qadir, M.T. van Vliet, V. Smakhtin, S.-m. Kang, The state of desalination and
496 brine production: A global outlook, Science of the Total Environment, (2018).

497 [4] B. Van der Bruggen, C. Vandecasteele, Removal of pollutants from surface water and
498 groundwater by nanofiltration: overview of possible applications in the drinking water
499 industry, Environmental pollution, 122 (2003) 435-445.

500 [5] M.W. Shahzad, M. Burhan, L. Ang, K.C. Ng, Energy-water-environment nexus
501 underpinning future desalination sustainability, Desalination, 413 (2017) 52-64.

502 [6] S. Lee, J. Choi, Y.-G. Park, H. Shon, C.H. Ahn, S.-H. Kim, Hybrid desalination processes
503 for beneficial use of reverse osmosis brine: Current status and future prospects, Desalination,
504 454 (2019) 104-111.

505 [7] H.B. Park, J. Kamcev, L.M. Robeson, M. Elimelech, B.D. Freeman, Maximizing the right
506 stuff: The trade-off between membrane permeability and selectivity, Science, 356 (2017)
507 eaab0530.

508 [8] L.Y. Ng, A.W. Mohammad, C.P. Leo, N. Hilal, Polymeric membranes incorporated with
509 metal/metal oxide nanoparticles: a comprehensive review, Desalination, 308 (2013) 15-33.

510 [9] W. Lau, A. Ismail, N. Misdan, M. Kassim, A recent progress in thin film composite
511 membrane: a review, Desalination, 287 (2012) 190-199.

512 [10] S. Hermans, R. Bernstein, A. Volodin, I.F. Vankelecom, Study of synthesis parameters
513 and active layer morphology of interfacially polymerized polyamide–polysulfone membranes,
514 Reactive and Functional Polymers, 86 (2015) 199-208.

515 [11] Z. Fan, Z. Wang, N. Sun, J. Wang, S. Wang, Performance improvement of polysulfone
516 ultrafiltration membrane by blending with polyaniline nanofibers, Journal of Membrane
517 Science, 320 (2008) 363-371.

518 [12] Y. Mansourpanah, S. Madaeni, A. Rahimpour, M. Adeli, M. Hashemi, M. Moradian,
519 Fabrication new PES-based mixed matrix nanocomposite membranes using polycaprolactone
520 modified carbon nanotubes as the additive: property changes and morphological studies,
521 Desalination, 277 (2011) 171-177.

522 [13] H. Zhao, L. Wu, Z. Zhou, L. Zhang, H. Chen, Improving the antifouling property of
523 polysulfone ultrafiltration membrane by incorporation of isocyanate-treated graphene oxide,
524 Physical Chemistry Chemical Physics, 15 (2013) 9084-9092.

525 [14] E.M. Hoek, A.K. Ghosh, X. Huang, M. Liong, J.I. Zink, Physical–chemical properties,
526 separation performance, and fouling resistance of mixed-matrix ultrafiltration membranes,
527 Desalination, 283 (2011) 89-99.

528 [15] S. Zhao, Z. Wang, X. Wei, X. Tian, J. Wang, S. Yang, S. Wang, Comparison study of the
529 effect of PVP and PANI nanofibers additives on membrane formation mechanism, structure
530 and performance, Journal of membrane science, 385 (2011) 110-122.

531 [16] J.M. Arsuaga, A. Sotto, G. del Rosario, A. Martínez, S. Molina, S.B. Teli, J. de Abajo,
532 Influence of the type, size, and distribution of metal oxide particles on the properties of
533 nanocomposite ultrafiltration membranes, Journal of membrane science, 428 (2013) 131-141.

534 [17] P. Daraei, S.S. Madaeni, N. Ghaemi, E. Salehi, M.A. Khadivi, R. Moradian, B. Astinchap,
535 Novel polyethersulfone nanocomposite membrane prepared by PANI/Fe3O4 nanoparticles

with enhanced performance for Cu (II) removal from water, Journal of Membrane Science, 415 (2012) 250-259.

[18] A. Rahimpour, S. Madaeni, A. Taheri, Y. Mansourpanah, Coupling TiO2 nanoparticles with UV irradiation for modification of polyethersulfone ultrafiltration membranes, Journal of Membrane Science, 313 (2008) 158-169.

[19] A. Berezhkovskii, G. Hummer, Single-file transport of water molecules through a carbon nanotube, Phys Rev Lett, 89 (2002) 064503.

[20] S. Casanova, M.K. Borg, Y.J. Chew, D. Mattia, Surface-controlled water flow in nanotube membranes, ACS applied materials & interfaces, 11 (2018) 1689-1698.

[21] M. Elimelech, W.A. Phillip, The future of seawater desalination: energy, technology, and the environment, science, 333 (2011) 712-717.

[22] D. Mattia, H. Leese, K.P. Lee, Carbon nanotube membranes: from flow enhancement to permeability, Journal of Membrane Science, 475 (2015) 266-272.

[23] M. Majumder, N. Chopra, B.J. Hinds, Effect of Tip Functionalization on Transport through Vertically Oriented Carbon Nanotube Membranes, J. Am. Chem. Soc., 127 (2005) 9062-9070.

[24] K.P. Lee, T.C. Arnot, D. Mattia, A review of reverse osmosis membrane materials for desalination—development to date and future potential, Journal of Membrane Science, 370 (2011) 1-22.

[25] M. Baghbanzadeh, D. Rana, C.Q. Lan, T. Matsuura, Effects of inorganic nano-additives on properties and performance of polymeric membranes in water treatment, Separation & Purification Reviews, 45 (2016) 141-167.

[26] Z.-X. Low, J. Ji, D. Blumenstock, Y.-M. Chew, D. Wolverson, D. Mattia, Fouling resistant 2D boron nitride nanosheet – PES nanofiltration membranes, Journal of Membrane Science, 563 (2018) 949-956.

[27] F. Xiao, B. Wang, X. Hu, S. Nair, Y. Chen, Thin film nanocomposite membrane containing zeolitic imidazolate framework-8 via interfacial polymerization for highly permeable nanofiltration, Journal of the Taiwan Institute of Chemical Engineers, 83 (2018) 159-167.

[28] H. Zhao, S. Qiu, L. Wu, L. Zhang, H. Chen, C. Gao, Improving the performance of polyamide reverse osmosis membrane by incorporation of modified multi-walled carbon nanotubes, Journal of Membrane Science, 450 (2014) 249-256.

[29] J. Yin, G. Zhu, B. Deng, Multi-walled carbon nanotubes (MWNTs)/polysulfone (PSU) mixed matrix hollow fiber membranes for enhanced water treatment, Journal of membrane science, 437 (2013) 237-248.

[30] C.C. Yu, H.W. Yu, Y.X. Chu, H.M. Ruan, J.N. Shen, Preparation thin film nanocomposite membrane incorporating PMMA modified MWNT for nanofiltration, in: Key Engineering Materials, Trans Tech Publ, 2013, pp. 882-886.

[31] H. Wu, B. Tang, P. Wu, MWNTs/polyester thin film nanocomposite membrane: an approach to overcome the trade-off effect between permeability and selectivity, The Journal of Physical Chemistry C, 114 (2010) 16395-16400.

[32] W.-F. Chan, H.-y. Chen, A. Surapathi, M.G. Taylor, X. Shao, E. Marand, J.K. Johnson, Zwitterion functionalized carbon nanotube/polyamide nanocomposite membranes for water desalination, Acs Nano, 7 (2013) 5308-5319.

580 [33] J. Park, W. Choi, S.H. Kim, B.H. Chun, J. Bang, K.B. Lee, Enhancement of chlorine
581 resistance in carbon nanotube based nanocomposite reverse osmosis membranes, Desalination
582 and Water Treatment, 15 (2010) 198-204.

583 [34] D. Golberg, Y. Bando, Y. Huang, T. Terao, M. Mitome, C. Tang, C. Zhi, Boron nitride
584 nanotubes and nanosheets, ACS nano, 4 (2010) 2979-2993.

585 [35] M. Suk, A. Raghunathan, N. Aluru, Fast reverse osmosis using boron nitride and carbon
586 nanotubes, Applied Physics Letters, 92 (2008) 133120.

587 [36] C.Y. Won, N. Aluru, Water permeation through a subnanometer boron nitride nanotube,
588 Journal of the American Chemical Society, 129 (2007) 2748-2749.

589 [37] E. Secchi, S. Marbach, A. Niguès, D. Stein, A. Siria, L. Bocquet, Massive radius-
590 dependent flow slippage in carbon nanotubes, Nature, 537 (2016) 210-213.

591 [38] J. Sokoloff, Enhancement of the water flow velocity through carbon nanotubes resulting
592 from the radius dependence of the friction due to electron excitations, Physical Review E, 97
593 (2018) 033107.

594 [39] T.A. Hilder, D. Gordon, S.H. Chung, Salt rejection and water transport through boron
595 nitride nanotubes, Small, 5 (2009) 2183-2190.

596 [40] A. Siria, P. Poncharal, A.-L. Biance, R. Fulcrand, X. Blase, S.T. Purcell, L. Bocquet, Giant
597 osmotic energy conversion measured in a single transmembrane boron nitride nanotube,
598 Nature, 494 (2013) 455.

599 [41] H. Lim, B.L. Suh, M.J. Kim, H. Yun, J. Kim, B.J. Kim, S.G. Jang, High-performance,
600 recyclable ultrafiltration membranes from P4VP-assisted dispersion of flame-resistive boron
601 nitride nanotubes, Journal of membrane science, 551 (2018) 172-179.

602 [42] X. Lin, Q. Yang, L. Ding, B. Su, Ultrathin silica membranes with highly ordered and
603 perpendicular nanochannels for precise and fast molecular separation, ACS nano, 9 (2015)
604 11266-11277.

605 [43] C.H. Lee, J. Wang, V.K. Kayatsha, J.Y. Huang, Y.K. Yap, Effective growth of boron
606 nitride nanotubes by thermal chemical vapor deposition, Nanotechnology, 19 (2008) 455605.

607 [44] M. Crimp, D. Oppermann, K. Krehbiel, Suspension properties of hexagonal BN powders:
608 effect of pH and oxygen content, Journal of materials science, 34 (1999) 2621-2625.

609 [45] R.Y. Tay, H. Li, S.H. Tsang, L. Jing, D. Tan, M. Wei, E.H.T. Teo, Facile Synthesis of
610 Millimeter-Scale Vertically Aligned Boron Nitride Nanotube Forests by Template-Assisted
611 Chemical Vapor Deposition, Chemistry of Materials, 27 (2015) 7156-7163.

612 [46] K.P. Lee, J. Zheng, G. Bargeman, A.J. Kemperman, N.E. Benes, pH stable thin film
613 composite polyamine nanofiltration membranes by interfacial polymerisation, Journal of
614 membrane science, 478 (2015) 75-84.

615 [47] G. Lai, W. Lau, P. Goh, Y. Tan, B. Ng, A. Ismail, A novel interfacial polymerization
616 approach towards synthesis of graphene oxide-incorporated thin film nanocomposite
617 membrane with improved surface properties, Arabian journal of chemistry, (2017).

618 [48] R.N. Wenzel, Surface roughness and contact angle, The Journal of Physical Chemistry,
619 53 (1949) 1466-1467.

620 [49] B. Liu, S. Yan, Z. Song, M. Liu, X. Ji, W. Yang, J. Liu, One-step synthesis of boron nitride
621 quantum dots: Simple chemistry meets delicate nanotechnology, Chemistry–A European
622 Journal, 22 (2016) 18899-18907.

623 [50] C.Y. Tang, Y.-N. Kwon, J.O. Leckie, Probing the nano-and micro-scales of reverse
624 osmosis membranes—A comprehensive characterization of physiochemical properties of
625 uncoated and coated membranes by XPS, TEM, ATR-FTIR, and streaming potential
626 measurements, Journal of Membrane Science, 287 (2007) 146-156.

627 [51] A. Celik-Aktas, J.-M. Zuo, J.F. Stubbins, C. Tang, Y. Bando, Double-helix structure in
628 multiwall boron nitride nanotubes, Acta Crystallographica Section A: Foundations of
629 Crystallography, 61 (2005) 533-541.

630 [52] B.J. Hinds, N. Chopra, T. Rantell, R. Andrews, V. Gavalas, L.G. Bachas, Aligned
631 multiwalled carbon nanotube membranes, Science, 303 (2004) 62-65.

632 [53] T. Chen, J. Xiao, G. Yang, Cubic boron nitride with an intrinsic peroxidase-like activity,
633 RSC Advances, 6 (2016) 70124-70132.

634 [54] N. Saha, S. Joshi, Performance evaluation of thin film composite polyamide nanofiltration
635 membrane with variation in monomer type, Journal of Membrane Science, 342 (2009) 60-69.

636 [55] F. Mirabella Jr, Practical spectroscopy series, Internal Reflection Spectroscopy: Theory
637 and Applications, (1993) 17-52.

638 [56] B. Zhong, X. Huang, G. Wen, H. Yu, X. Zhang, T. Zhang, H. Bai, Large-scale fabrication
639 of boron nitride nanotubes via a facile chemical vapor reaction route and their
640 cathodoluminescence properties, Nanoscale Res Lett, 6 (2011) 36.

641 [57] W. Laosamathikul, T. Sawada, T. Serizawa, Alcoholysis-Assisted Exfoliation of Boron
642 Nitride Nanosheets from Hexagonal Boron Nitride, Transactions of the Materials Research
643 Society of Japan, 42 (2017) 135-138.

644 [58] M.L. Lind, D. Eumine Suk, T.-V. Nguyen, E.M. Hoek, Tailoring the structure of thin film
645 nanocomposite membranes to achieve seawater RO membrane performance, Environmental
646 science & technology, 44 (2010) 8230-8235.

647 [59] S. Roy, S.A. Ntim, S. Mitra, K.K. Sirkar, Facile fabrication of superior nanofiltration
648 membranes from interfacially polymerized CNT-polymer composites, Journal of Membrane
649 Science, 375 (2011) 81-87.

650 [60] J.S. Taurozzi, C.A. Crock, V.V. Tarabara, C60-polysulfone nanocomposite membranes:
651 entropic and enthalpic determinants of C60 aggregation and its effects on membrane properties,
652 Desalination, 269 (2011) 111-119.

653 [61] B.-H. Jeong, E.M. Hoek, Y. Yan, A. Subramani, X. Huang, G. Hurwitz, A.K. Ghosh, A.
654 Jawor, Interfacial polymerization of thin film nanocomposites: a new concept for reverse
655 osmosis membranes, Journal of membrane science, 294 (2007) 1-7.

656 [62] J. Yin, E.-S. Kim, J. Yang, B. Deng, Fabrication of a novel thin-film nanocomposite (TFN)
657 membrane containing MCM-41 silica nanoparticles (NPs) for water purification, Journal of
658 membrane science, 423 (2012) 238-246.

659 [63] F. Fornasiero, H.G. Park, J.K. Holt, M. Stadermann, C.P. Grigoropoulos, A. Noy, O.
660 Bakajin, Ion exclusion by sub-2-nm carbon nanotube pores, Proceedings of the National
661 Academy of Sciences, 105 (2008) 17250-17255.

662 [64] S.G. Kim, D.H. Hyeon, J.H. Chun, B.-H. Chun, S.H. Kim, Nanocomposite poly (arylene
663 ether sulfone) reverse osmosis membrane containing functional zeolite nanoparticles for
664 seawater desalination, Journal of membrane science, 443 (2013) 10-18.

665 [65] S.-M. Xue, Z.-L. Xu, Y.-J. Tang, C.-H. Ji, Polypiperazine-amide nanofiltration membrane
666 modified by different functionalized multiwalled carbon nanotubes (MWCNTs), ACS applied
667 materials & interfaces, 8 (2016) 19135-19144.

668 [66] H.-Z. Zhang, Z.-L. Xu, H. Ding, Y.-J. Tang, Positively charged capillary nanofiltration
669 membrane with high rejection for Mg2+ and Ca2+ and good separation for Mg2+ and Li+,
670 Desalination, 420 (2017) 158-166.

671 [67] J. nan Shen, C. chao Yu, H. min Ruan, C. jie Gao, B. Van der Bruggen, Preparation and
672 characterization of thin-film nanocomposite membranes embedded with poly (methyl
673 methacrylate) hydrophobic modified multiwalled carbon nanotubes by interfacial
674 polymerization, Journal of membrane science, 442 (2013) 18-26.

675